MnSn2 electrodes for Li-ion batteries: Mechanisms at the nano scale and electrode/electrolyte interface

Bertrand Philippe, A. Mahmoud, Jean-Bernard Ledeuil, Moulay Tahar Sougrati, K. Edström, Rémi Dedryvère, Danielle Gonbeau, P.E. Lippens

To cite this version:

Bertrand Philippe, A. Mahmoud, Jean-Bernard Ledeuil, Moulay Tahar Sougrati, K. Edström, et al.. MnSn2 electrodes for Li-ion batteries: Mechanisms at the nano scale and electrode/electrolyte interface. Electrochimica Acta, 2014, 123, pp.72-83. ⟨10.1016/j.electacta.2014.01.010⟩. ⟨hal-01016124⟩

HAL Id: hal-01016124
https://hal.science/hal-01016124v1

Submitted on 13 Feb 2025

$MnSn_2$ electrodes for Li-ion batteries: mechanisms at the nano scale and electrode/electrolyte interface

B. Philippe [1,2,4], A. Mahmoud [3], J.-B. Ledeuil [1], M. T. Sougrati [3,4,5], K. Edström [2,4],
R. Dedryvère [1,4,5,*], D. Gonbeau [1,4,5], P.-E. Lippens [3,4,5,*]

[1] IPREM/ECP (CNRS UMR 5254), University of Pau, Hélioparc, 2 av. Pierre Angot, 64053 Pau cedex 9, France
[2] Dept. of Chemistry, Ångström Lab., Uppsala University, Box 538, SE-75121 Uppsala, Sweden
[3] Institut Charles Gerhardt (CNRS UMR 5253), AIME, Université Montpellier II, Place Eugène Bataillon, 34095 Montpellier cedex 5, France
[4] Alistore - European Research Institute, 33 rue Saint-Leu, 80039 Amiens cedex, France
[5] Réseau sur le Stockage Electrochimique de l'Energie (RS2E), FR CNRS 3459, France

Abstract

We have investigated the reaction mechanisms occurring upon the first discharge/charge cycle of a $MnSn_2$ // Li electrochemical cell, by using bulk- and surface-sensitive characterization techniques (X-ray Diffraction, ^{119}Sn Mössbauer spectroscopy, magnetic measurements, X-ray photoelectron and Auger spectroscopies). Compared to other tin-transition metal alloys, $MnSn_2$ displays an original behaviour. Lithium insertion into $MnSn_2$ particles results in a nanocomposite consisting of Li_7Sn_2 phase, and of Mn nanoparticles which are immediately oxidized at their surface. Lithium extraction from this nanocomposite leads to the formation of magnetic $MnSn_2$ particles and to our knowledge it is the first time such a mechanism is observed in tin-based intermetallic electrode materials due to electrochemical reaction with Li. The solid electrolyte interphase (SEI) is formed at the beginning of the first discharge and its thickness slightly increases upon further lithium insertion. A partial re-dissolution process occurs upon lithium extraction from the material, while its chemical composition is very stable over the whole cycle.

Keywords: Lithium-ion batteries, $MnSn_2$, tin, intermetallics, Mössbauer, XPS, magnetism

* corresponding authors: remi.dedryvere@univ-pau.fr, lippens@univ-montp2.fr

1. Introduction

Lithium-ion (Li-ion) batteries are today the most interesting power source for portable electronic devices, and are one of the most promising candidates for propulsion of electric (or hybrid) vehicles and storage of renewable electric energy. A great challenge to meet the specifications for new applications is to enhance the performances of electrode materials in terms of reversible capacity, cycling stability, energy and power density, and safety.[1,2]

In current commercial Li-ion batteries, negative electrode materials are made up of carbonaceous intercalation materials. Graphitic carbon displays a theoretical gravimetric capacity of 372 mAh/g which corresponds to the intercalation of one lithium atom per six carbon atoms (LiC_6). Many studies are today devoted to the replacement of carbonaceous electrodes to reach higher capacities. Metals and semimetals (M = Si, Ge, Sn, Sb, etc.) have the ability to react with much more lithium because they can electrochemically and reversibly form lithium-metal alloys Li_xM according to equation (1). [3]

$$M + x\,Li^+ + x\,e^- \leftrightarrow Li_xM \qquad (1)$$

These elements present high volumetric and gravimetric capacities and low working potentials *vs.* Li^+/Li, *i.e.* two key parameters for a good Li-ion negative electrode material. [4] Among them, tin can form up to seven Li_xSn alloys with different compositions: Li_2Sn_5, LiSn, Li_7Sn_3, Li_5Sn_2, $Li_{13}Sn_5$, Li_7Sn_2 and $Li_{22}Sn_5$. [5] The alloying potentials of these species are higher than that of graphite, which is important for the safety of the battery because it avoids lithium electroplating. The lithium-richer alloy $Li_{22}Sn_5$ ($Li_{4.4}Sn$) corresponds to a high theoretical capacity (993 mAh/g). Actually this composition is rarely reached in practical conditions, and Li_7Sn_2 appears to be the maximum composition in lithium batteries, [6] which still corresponds to a more than twice greater theoretical capacity than graphite (790 mAh/g).

However, the huge volume expansion accompanying lithium uptake and formation of these alloys (around 260 % for $Li_{22}Sn_5$) is the main problem for these materials. This expansion leads to high mechanical strains that cause the loss of electrical contact between particles, and consequently, to the capacity fading upon electrochemical cycling. [7,8] In order to reduce the volume expansion, one strategy is to use M-Sn alloys, where M is an electrochemically inactive metal towards lithium which plays the role of a matrix buffering the volume expansion. [7] Various Sn-based intermetallic compounds have been studied, for example $NbSn_2$,[9] Al-Sn,[10] $FeSn_2$,[11,12] Ni_3Sn_4, [13,14,15] $CoSn_2$,[6,16] Cu_6Sn_5[17,18,19,20] or $CrSn_2$[16] and only few studies have been done using manganese as inactive metal.[21,22] These materials, however, still display too poor electrochemical behaviors to be used now as an alternative to carbon electrodes. Research efforts to understand these limitations have been focused on Li-Sn alloying processes and structural changes undergone upon lithium uptake/removal.[23,24] Some differences can be observed as a function of the inactive metal nature, resulting in different shapes of voltage *vs.* capacity discharge/charge curves.

In a previous paper, we have investigated the influence of the synthesis procedure of $MnSn_2$ compound on its electrochemical performances in $MnSn_2$ // Li cells. [25] In the present paper, we report the investigation of Li-Sn alloying/de-alloying processes occurring upon lithiation/delithiation of $MnSn_2$ electrodes. A step by step analysis of the first electrochemical cycle has been carried out by X-ray diffraction (XRD), ^{119}Sn Mössbauer Spectroscopy (both in *operando* mode), X-ray photoelectron spectroscopy (XPS) and magnetic measurements. The study of the electrode/electrolyte interface (the SEI, *i.e.* Solid Electrolyte Interphase) was also performed.

2. Experimental details

2.1. Material synthesis

$MnSn_2$ was prepared by solid state synthesis from micrometric tin (Sigma Aldrich, 99.5% purity) and manganese (Sigma Aldrich, 99.5% purity) powders, as described elsewhere.[25] The stoichiometric amounts of powders (1.5 g) were charged in a 50 mL stainless steel grinding jar within an argon-filled glove box. The mixture was first mechanically milled (with a planetary ball mill) with four stainless steel balls of 5 g each during 3 days at 400 rpm. To avoid high temperature produced during long time milling, the process was paused for 10 min every 15 min. The obtained powder was then wrapped under argon atmosphere, sealed in a quartz tube under dynamic vacuum, heated at 500°C for 15 days and cooled down rapidly by water quenching to obtain a final black product.

2.2. Electrochemical cycling

The electrodes for XRD and Mössbauer analyses were prepared by mixing 80 wt.% of $MnSn_2$ active material with 10 wt.% of carbon black as electronic conductor and 10 wt.% of polyvinylidene fluoride (PVdF) as binder, dissolved in *n*-methyl pyrrolidinone. The mixture was spread onto a Cu foil substrate. The electrodes were pressed and dried for 12 h at 120 °C under vacuum to remove solvent and water. For XPS analyses no binder was used to make easier the characterization of carbonaceous species at the surface. The electrodes were prepared by mixing 90 wt.% of $MnSn_2$ with 10 wt.% of carbon black. The liquid electrolyte was $LiPF_6$ dissolved (1 mol/L) in a mixture of ethylene carbonate and dimethyl carbonate (EC:DMC 1:1), and a Li foil was used as the counter and reference electrode.

For *operando* experiments specific electrochemical cells were designed for recording XRD data in reflection mode [26] and Mössbauer data in transmission mode [27] during cycling without stopping the battery. For XPS experiments the electrochemical cycling was performed in standard Swagelok™ cells. All electrochemical cells were assembled in a glove box in controlled argon atmosphere.

Electrochemical cycles were carried out within a fixed voltage window, between 0.01 and 1.2 V *vs.* Li^+/Li^0, under galvanostatic conditions with a C/10 current rate (*i.e.* corresponding to the insertion of 1 Li per $MnSn_2$ formula unit in 10h).

2.3. Analytical techniques

XRD was carried out over the 2θ range from 10° to 90° by using a PHILIPS X'Pert MPD equipped with the X'celerator detector with Cu K_α radiation (λ=1.5418Å) and a nickel filter. The cell parameters were refined from the diffraction patterns using the FULLPROF program [28].

^{119}Sn Mössbauer spectra were recorded in transmission geometry and constant acceleration mode at room temperature with a 5 mCi $Ca^{119m}SnO_3$ source. The velocity scale was calibrated using the magnetic six-line spectrum of a high-purity iron foil absorber as a standard and using ^{57}Co(Rh) as the source. The values of the isomer shift, δ, quadrupole splitting, Δ, linewidth at half maximum, Γ, and relative area, A, were determined with a non-linear least-square method [29] and Lorentzian profiles. The isomer shift values are given with respect to $BaSnO_3$. The spectra were recorded continuously during the first discharge and the first charge. The data were collected every 2 hours, which corresponds to the reaction of 0.2 Li/$MnSn_2$ for each spectrum.

XPS Measurements were carried out with a Kratos Axis Ultra spectrometer (Kratos Analytical Ltd, Manchester, UK) using a focused monochromatized Al Kα radiation (hν = 1486.6 eV). The spectrometer was calibrated using the photoemission line Ag $3d_{5/2}$ (binding energy 368.3 eV). The full width at half maximum (FWHM) was 0.58 eV under the recording conditions. Core peak and valence spectra were recorded with a constant 20 eV pass energy. The analyzed area of the samples was 300×700 μm^2 and the pressure in the analysis chamber was around 5.10^{-9} mbar. The binding energy scale was calibrated by the hydrocarbon surface contamination C 1s peak at 285.0 eV. Core peaks were analyzed using a nonlinear Shirley-type background [30]. The peak positions and areas were optimized by a weighted least-square fitting method using 70 % Gaussian and 30 % Lorentzian lineshapes. Short acquisition time spectra were recorded as fingerprints at the beginning and at the end of each experiment to check that the samples did not suffer from X-ray beam degradation during the measurements. Quantification was performed on the basis of Scofield's relative sensitivity factors.[31] Additional measurements were carried out at BESSY II synchrotron facility (HIKE end station [32], KMC-1 beamline [33], Helmholtz Zentrum Berlin, Germany) with a fixed excitation energy was used (hν = 2300 eV).

After cycling experiments the $MnSn_2$ electrodes were carefully separated from the other battery components in argon atmosphere, soaked in ultrapure DMC solvent to dilute the salt and make the surface observable, and dried prior to being placed onto the XPS sample holder without any contamination.

Auger electron spectroscopy (AES) was carried out with a JEOL JAMP 9500F operating at the probe current of 4 nA and 15 keV and a working distance (source/sample) of about 24 mm. $MnSn_2$ powder was directly deposited onto an indium foil for analysis.

3. Results and discussion

3.1. Characterization of $MnSn_2$

The bulk characterization of the pristine $MnSn_2$ material by XRD and ^{119}Sn Mössbauer spectroscopy was already shown in a previous paper [25] and can be summarized as follows.

Bragg peaks of the XRD pattern could all be indexed in a primitive tetragonal structure (I 4/*mcm* space group) with $a = 6.63$Å and $c = 5.42$Å in agreement with previously reported structure of $MnSn_2$. [34] Rather narrow and symmetric Bragg lines were observed, indicating the good crystallinity of the $MnSn_2$ powder. There were no peaks due to oxides or to β-Sn (which is often present in $MnSn_2$ obtained by direct heating of metallic powders [35]), showing the purity of the material. The ^{119}Sn Mössbauer spectrum of the $MnSn_2$ powder could be fitted with only one doublet. There was no magnetic splitting due to transferred hyperfine field as observed for bulk antiferromagnetic compounds, [35] which shows the paramagnetic behavior of this compound at room temperature. No additional doublet due to tin oxide could be detected. To conclude, $MnSn_2$ samples do not contain significant amounts of β-Sn or oxide particles in the bulk. The particles are rather well crystallized although they do not developed antiferromagnetic ordering.

Surface analysis of $MnSn_2$ particles was carried out by XPS. The Sn $3d_{5/2}$ and Mn 2p spectra are shown in Figure 1. Two photon energies were used: hν = 1486.6 (in-house) and 2300 eV (synchrotron). The highest photon energy allows a deeper analysis of the sample. The Sn $3d_{5/2}$ spectrum consists of two components. The first one at 485.2 eV is assigned to metallic tin (Sn^0) of $MnSn_2$. The second at 486.9 eV is attributed to tin oxide SnO_2 (Sn^{4+}). The increase of the photon energy leads to a significant decrease of the relative amount of oxide from 64 to 25% of the Sn $3d_{5/2}$ signal, which allows attribution of this component to the outermost surface oxide layer. The Mn 2p spectra display a main peak at ~642 eV for Mn $2p_{3/2}$ (~653 eV for Mn $2p_{1/2}$) assigned to manganese oxide. The increase of the photon energy from 1486.6 to 2300 eV allows an additional weak component to appear at 638 eV, which is clearly assigned to metallic manganese located under the oxide layer. Since this component remains very weak, manganese is more oxidized than tin at the surface of the particles. Note that from XPS measurements the Sn/Mn ratio at the surface of the sample is 0.9 instead of 2 for the bulk $MnSn_2$. This can be explained by the higher oxygen affinity of manganese. Therefore Mn segregates to the surface of the particles.

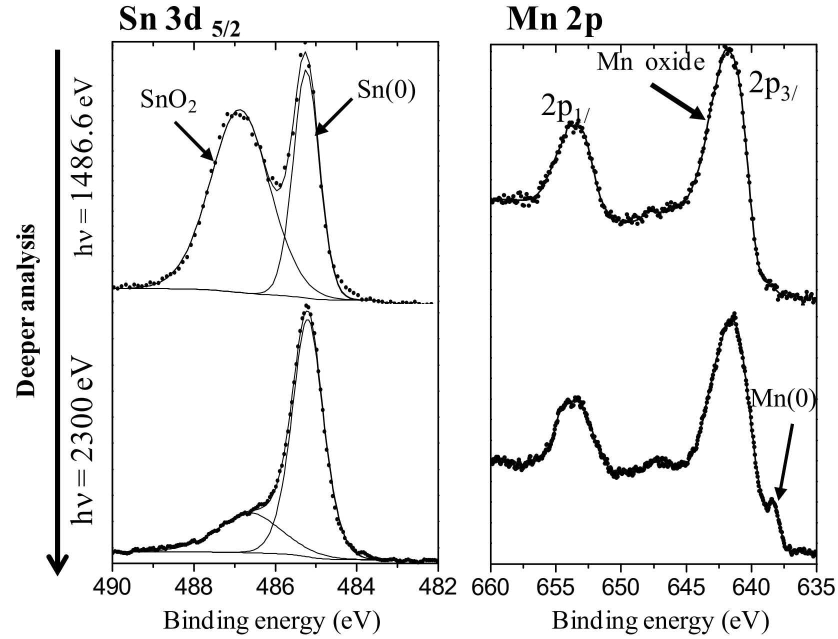

Figure 1: XPS Sn $3d_{5/2}$ and Mn 2p spectra of $MnSn_2$ powder recorded with two different photon energies: hν = 1486.6 and 2300 eV.

In order to complement the surface characterisation of the starting material, the $MnSn_2$ powder was examined by Auger Electron Spectroscopy (AES), which allows an elemental mapping of the surface (probe depth ~5 nm) with high lateral resolution. Figure 2 shows: (a) Scanning Electron Microscopy (SEM) imaging of a 40 µm diameter aggregate; (b) the Auger electron spectra of two selected ~20 nm diameter areas; (c), (d) and (e) Scanning Auger Microscopy (SAM) images of Sn, Mn and O elements, respectively, obtained by selection of their characteristic Auger kinetic energies. In the AES spectra the three elements are easily recognizable by their Sn MNN (426 and 435 eV), Mn LMM (533, 580 and 631 eV) and

O KLL (487 and 506 eV) main Auger peaks. Adsorbed carbonaceous species at the surface are also detectable by their C KLL peak. Mn and Sn SAM images (c) and (d) allow evidencing a non-uniform distribution of these two elements at the surface.

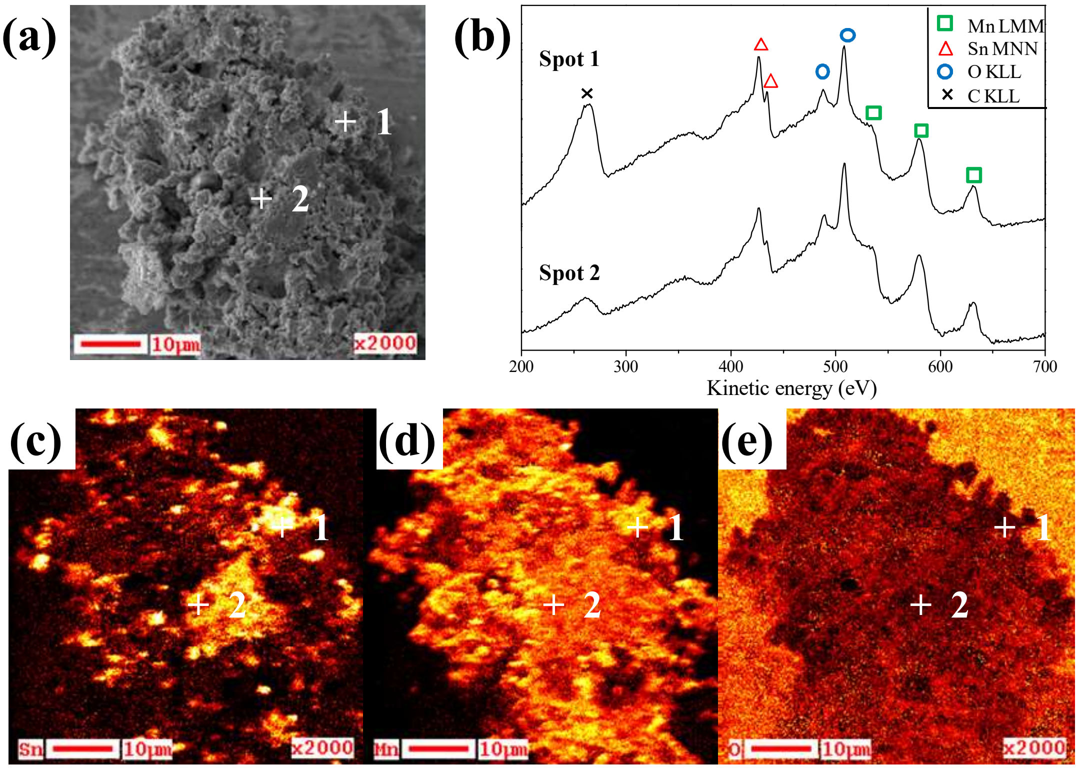

Figure 2: **(a)** SEM image of a 40 µm diameter $MnSn_2$ aggregate; **(b)** Auger Electron Spectra (AES) of two selected ~20 nm diameter areas; **(c)**, **(d)** and **(e)** Scanning Auger Microscopy (SAM) images of Sn, Mn and O elements, respectively, obtained by selection of their characteristic Auger kinetic energy signals.

Besides, the SAM image of oxygen shows no significant difference in the O KLL signal intensity, and therefore the intensity differences observed for Mn and Sn are not due to topographical effects of the surface, but actually to differences in the chemical composition at the surface. It is to be noted that these chemical heterogeneity only concerns the outermost surface of the particles, since bulk characterization of the material did not evidence unreacted metals nor separated oxide particles. However, this chemical state of the surface may have consequences concerning the reactivity of the electrode towards the electrolyte in a battery.

3.2. Study of the first electrochemical cycle

3.2.1. Electronic and structural mechanisms

Operando XRD patterns collected during insertion of Li into $MnSn_2$ (*i.e.* the first discharge of a $MnSn_2$//Li electrochemical cell) are shown in Figure 3a in the 2θ range 10-46°. The peaks at 36°, 40.5° and 42° are due to the beryllium window of the electrochemical cell and their intensities do no change during the lithiation of the electrode. The intensity of all the peaks of $MnSn_2$ decreases with increasing Li amount as clearly observed for the two 211 (34.2°) and 310 (42.8°) main Bragg peaks. Broad structures increase around 23° that can be assigned to lithium-rich Li-Sn compounds but the exact composition cannot be determined from XRD patterns. As shown in Figure 3b, the areas of the two main $MnSn_2$ peaks linearly decrease while those of Li-rich Li-Sn linearly increase as a function of the number of lithium x, for x greater than about 1 Li. There is a small angle shift of $MnSn_2$ lines toward higher values (<0.1°) that could be related to a small contraction of the cell maybe due to the decreasing size of the $MnSn_2$ particles. No variations were observed for the Li-Sn peak positions. The (112) Bragg peak of $MnSn_2$ at 38.2° partially overlaps with a peak of Li-Sn, which results in the decrease of a rather thin peak followed by the increase of a rather large structure in this range of angles. The size of the coherent domains (Figure 3c) was evaluated by Scherrer's law and shows a linear decrease for $MnSn_2$ from about 100 to 30 nm whereas the size slightly increases up to 20 nm for Li-Sn. Thus, the variations of the XRD patterns indicate that the lithiation of $MnSn_2$ negative electrode does not affect the active material up to about 1 Li and then transforms $MnSn_2$ into Li-Sn nanoalloys.

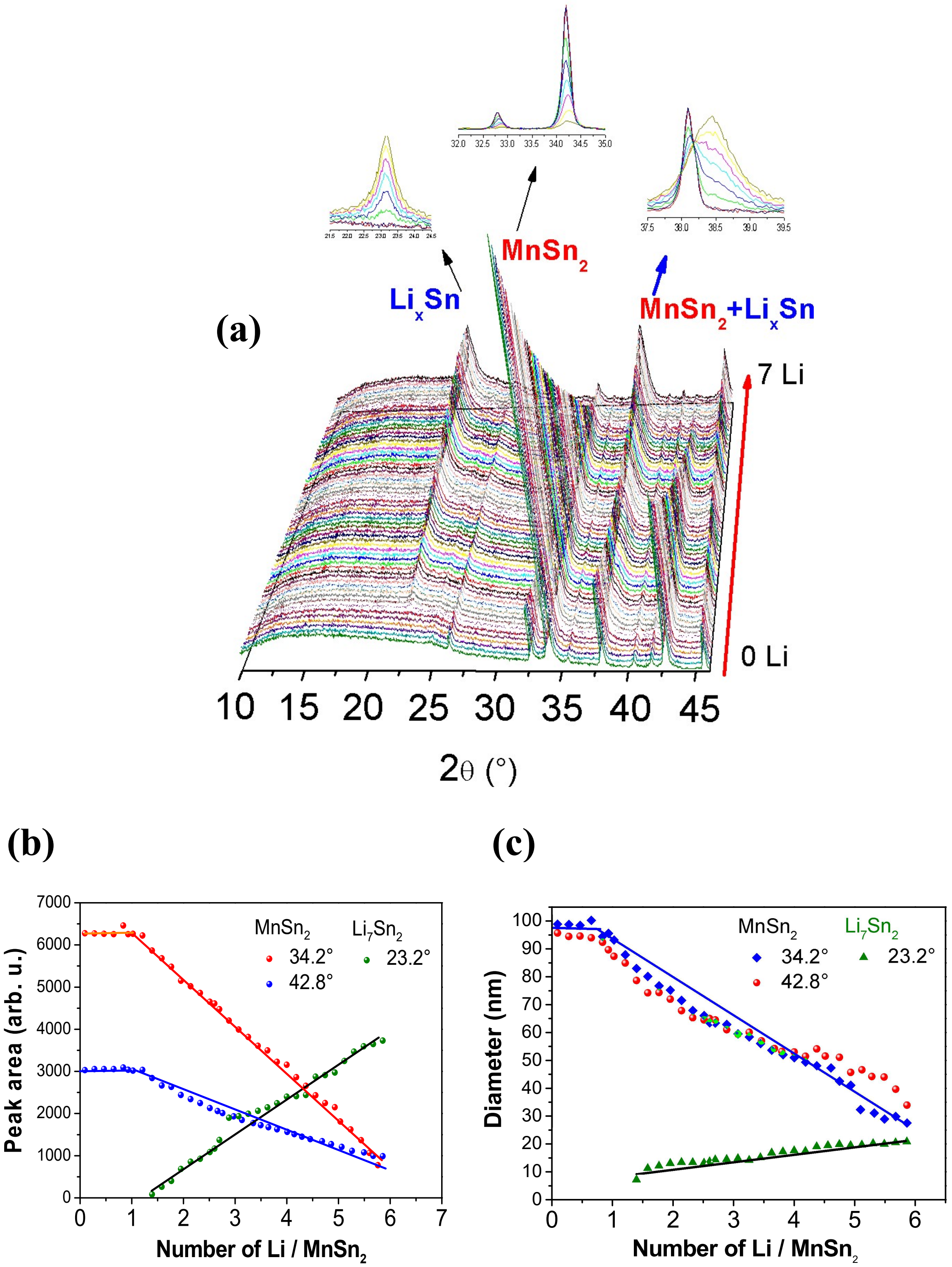

Figure 3: XRD data recorded in *operando* mode upon the first dicharge of a $MnSn_2$ // Li cell: **(a)** XRD patterns (Cu K_α =1.5418Å), **(b)** Peak areas of characteristic XRD lines of $MnSn_2$ and Li_7Sn_2 phases, **(c)** Coherent domain size of $MnSn_2$ and Li_7Sn_2 phases.

In order to obtain more information on electrochemically formed Li-Sn alloys, ^{119}Sn Mössbauer spectra were recorded upon the first discharge of a $MnSn_2$ // Li cell in *operando* mode, as shown in Figure 4b. The plotted spectra correspond to the points highlighted in the discharge curve of Figure 4a.

The first discharge displays two steps. In the first one (from 0 to 1 Li), the potential rapidly drops to 0.3 V. This part is generally attributed to the reduction of surface oxides by lithium and to the formation of the solid electrolyte interphase (SEI) layer.[36,37] The second step (from 1 to 7.7 Li) is expected to correspond to the formation of the Li_xSn alloy. An interesting feature is observed upon charge. Two voltage plateaus are observed: a first one at 0.6 V (x=7.7 to 3.6 Li) and a second one at 0.75 V (x=3.6 to 2.2 Li). The existence of two plateaus upon charge while only one is observed upon discharge shows that the mechanism occurring upon charge is not only a simple de-alloying process of the Li-Sn alloy formed upon discharge.

At the beginning of discharge the Mössbauer spectra consist of a doublet which is characteristic of nanostructured $MnSn_2$ (δ = 2.27 mm/s, Δ = 1.08 mm/s). During discharge the spectra progressively change to a more complicated shape that can only be fitted by adding a second unresolved doublet to account for Li-Sn alloys formed during the lithiation process. Although the spectrum obtained at the end of discharge can be fitted with one doublet, a better fit is obtained by considering an additional doublet assigned to $MnSn_2$. The existence of $MnSn_2$ at the end of discharge is due to incomplete lithiation of the electrode as also observed by XRD. The Mössbauer parameters of the main doublet (relative area of 90%) at the end of discharge are δ = 1.89 mm/s, Δ = 0.42 mm/s. These values are close to those of Li_7Sn_2 reference compound when fitted with a single doublet.[38] The relative area of the $MnSn_2$ sub-spectrum to the total spectrum is about 10% at the end of discharge.

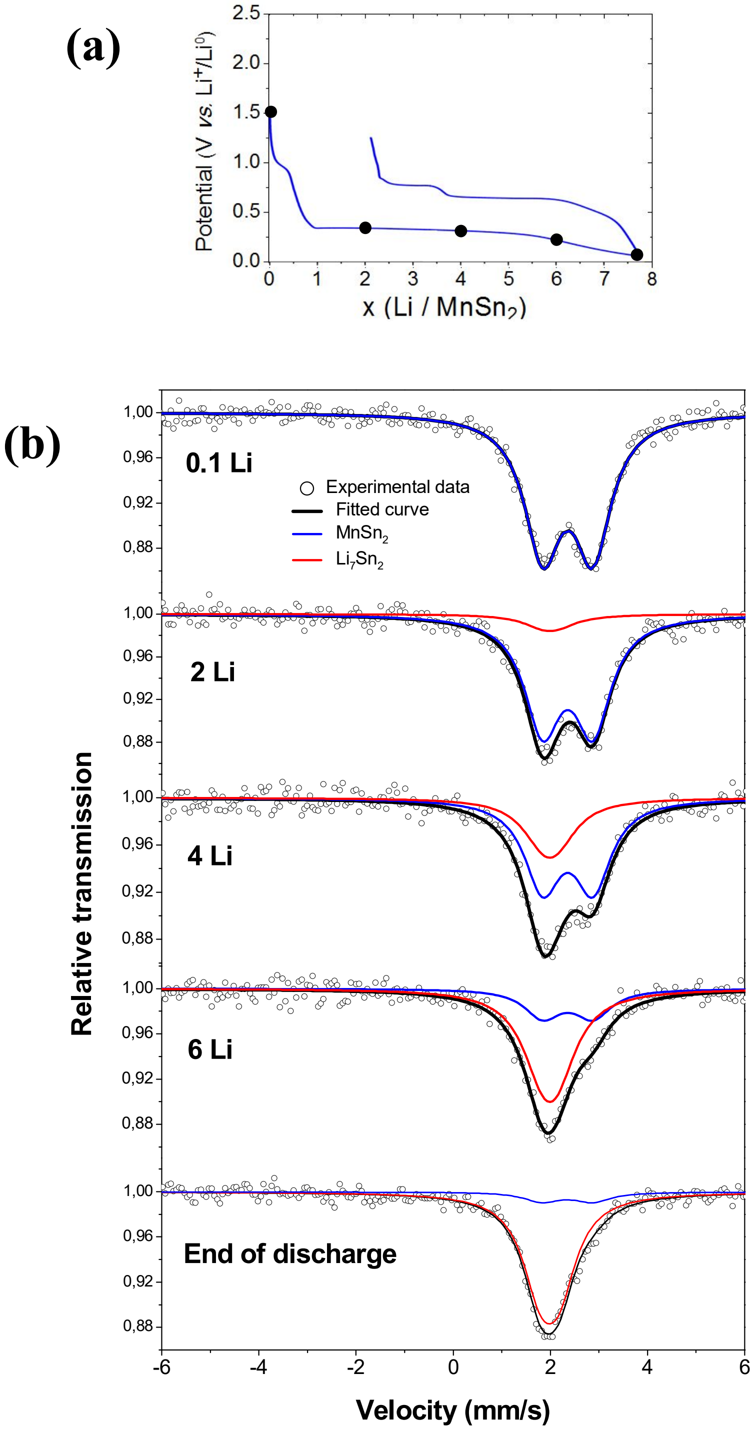

Figure 4: **(a)** First discharge/charge cycle of the $MnSn_2$//Li *operando* electrochemical cell, **(b)** ^{119}Sn Mössbauer data recorded in *operando* mode. The spectra correspond to the points highlighted in the discharge curve.

All the other spectra collected during the discharge were successfully fitted with these two components by considering identical linewidths and the relative contributions of $MnSn_2$ and Li_7Sn_2 sub-spectra to the total spectra as free parameters. The relative amounts of $MnSn_2$ and Li_7Sn_2 in the electrode can be evaluated from these relative areas by considering the ratio between the Lamb-Mössbauer factors of these two compounds. [27] This ratio can be evaluated from the variations of the total area of the Mössbauer spectra as a function of the number of inserted lithium x, which has been found to decrease linearly for x>1.5 in the present case as expected from a two-phase reaction.

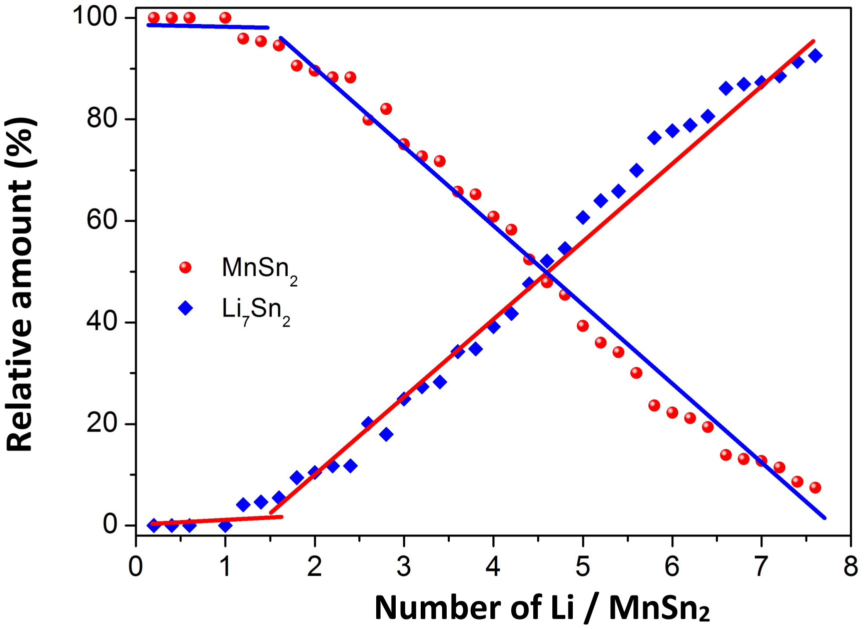

Figure 5: ^{119}Sn Mössbauer data recorded in *operando* mode upon the first discharge of a $MnSn_2$ // Li cell: Relative amounts of $MnSn_2$ and Li_7Sn_2 phases evaluated from Mössbauer spectra by taking into account the Lamb-Mössbauer factors.

A linear fit to the experimental data gives $f_{Li_7Sn_2}/f_{MnSn_2}$=0.62. For x >1.5 Li the relative amount of $MnSn_2$ linearly increases with x, whereas that of Li_7Sn_2 linearly decreases, as shown in Figure 5. This is a clear indication of the conversion reaction (2):

$$MnSn_2 + 7\ Li \rightarrow Mn + Li_7Sn_2 \qquad (2)$$

This reaction also suggests that the relative amount of manganese should linearly increase with the amount of Li.

Figure 6 shows the magnetic field dependence of the electrode magnetization at the end of the first discharge (x = 8Li) as a function of temperature. A high coercivity of about 230 mT is observed at 2 K and almost zero coercivity (<4 mT) at room temperature. Similar trends have been observed for Mn nanoparticles synthesized by arc-discharge and could be due to the existence of manganese oxides such as MnO or Mn_3O_4. [39]

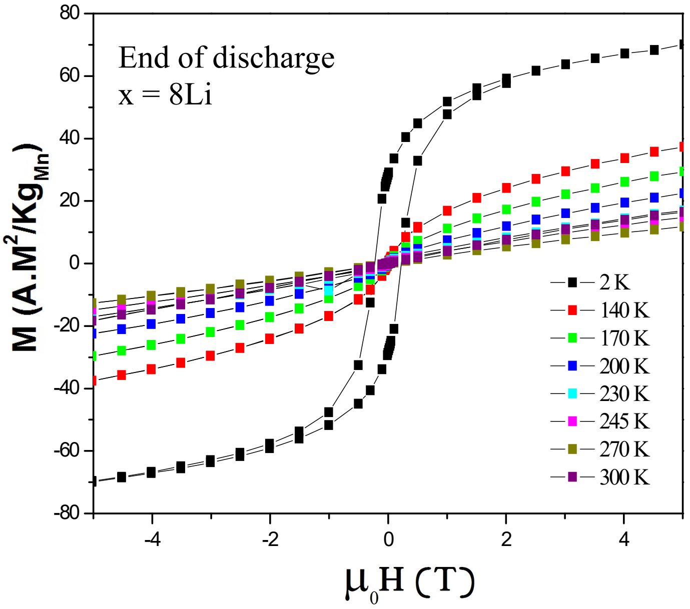

Figure 6: Magnetic measurements of the $MnSn_2$ electrode at the end of discharge (x = 8Li): magnetization *vs.* applied magnetic field hysteresis loops at different temperatures.

These results indicate the existence of manganese nanoparticles with oxide layer at the surface and/or manganese oxide nanoparticles at the end of discharge. This suggests that Mn atoms extruded from $MnSn_2$ during the lithiation form Mn nanoparticles that react with oxygen atoms found at the surface of the $MnSn_2$ as shown by XPS or in the electrolyte (reaction with solvent molecules). These results differ from those obtained with $FeSn_2$ based electrodes where iron oxides were not detected at the end of discharge from magnetic measurements [27].

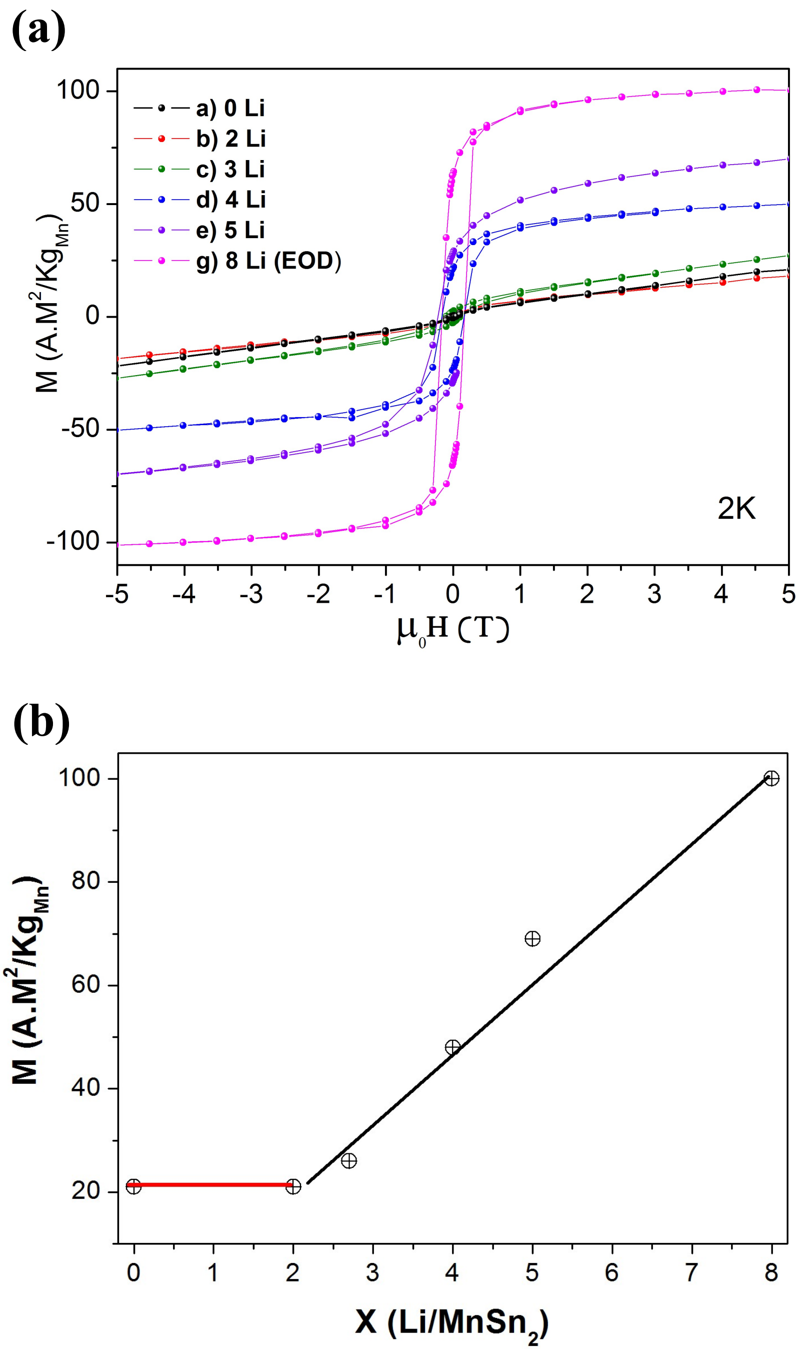

Figure 7: Magnetic measurements at T = 2 K of the $MnSn_2$ electrode upon discharge: **(a)** Magnetization *vs.* applied magnetic field hysteresis loops for different Li amounts, **(b)** Saturation magnetization *vs.* Li amount (for an applied field of 5T).

The low temperature (T=2 K) magnetization of the $MnSn_2$ electrode as a function of lithium number x was measured upon the first discharge (see Figure 7a). The saturation magnetization of the electrode (evaluated for an applied field of 5 T) shows a quasi-linear dependence on the lithium number x for x > 2 (see Figure 7b). Similar results were previously obtained for Ni_3Sn_4 or $CoSn_2$ based electrodes.[40] Such a linear increase is consistent with the linear increase of the number of Mn and/or Mn oxide nanoparticles during the conversion reaction. To conclude, $MnSn_2$ based electrode is progressively transformed into a nanocomposite formed by Li_7Sn_2 and Mn nanoparticles oxydized at surface during the first discharge.

This study was complemented by a characterisation of the electrode surface by XPS upon the first cycle. Figure 8 shows Sn $3d_{5/2}$ spectra of the $MnSn_2$ electrode at different electrochemical steps of the first discharge and charge. Corresponding points are reported in the electrochemical curve in the top right corner. Note that due to the specific formulation of the electrode without binder to facilitate the identification of carbonaceous species at the surface by XPS, only 6.5 Li are reached at the end of discharge, but with a low-voltage plateau beginning at 0.3 Li. At the beginning of discharge (sample B, x=0.5 Li) we can observe a decrease of the relative intensity of the tin oxide (SnO_2) component with respect to Sn^0, in good agreement with the reduction of the surface oxide into metallic tin upon lithium insertion. The Li-Sn alloying process has not started at this stage at the surface of the particles (neither in the bulk, as shown above). In the second part of the discharge (samples C to E, x=2.5 to 6.5 Li), three Sn $3d_{5/2}$ components are observed. The low binding energy peak at ~481 eV can be clearly attributed to the formation of the Li-Sn alloy. The weaker component at ~483 eV can be attributed to the unreacted $MnSn_2$ phase rather than to a lithium-poorer Li-

Sn alloy, since shifts of the starting phase component toward lower binding energies due to differential charging effects are commonly observed.[41,42]

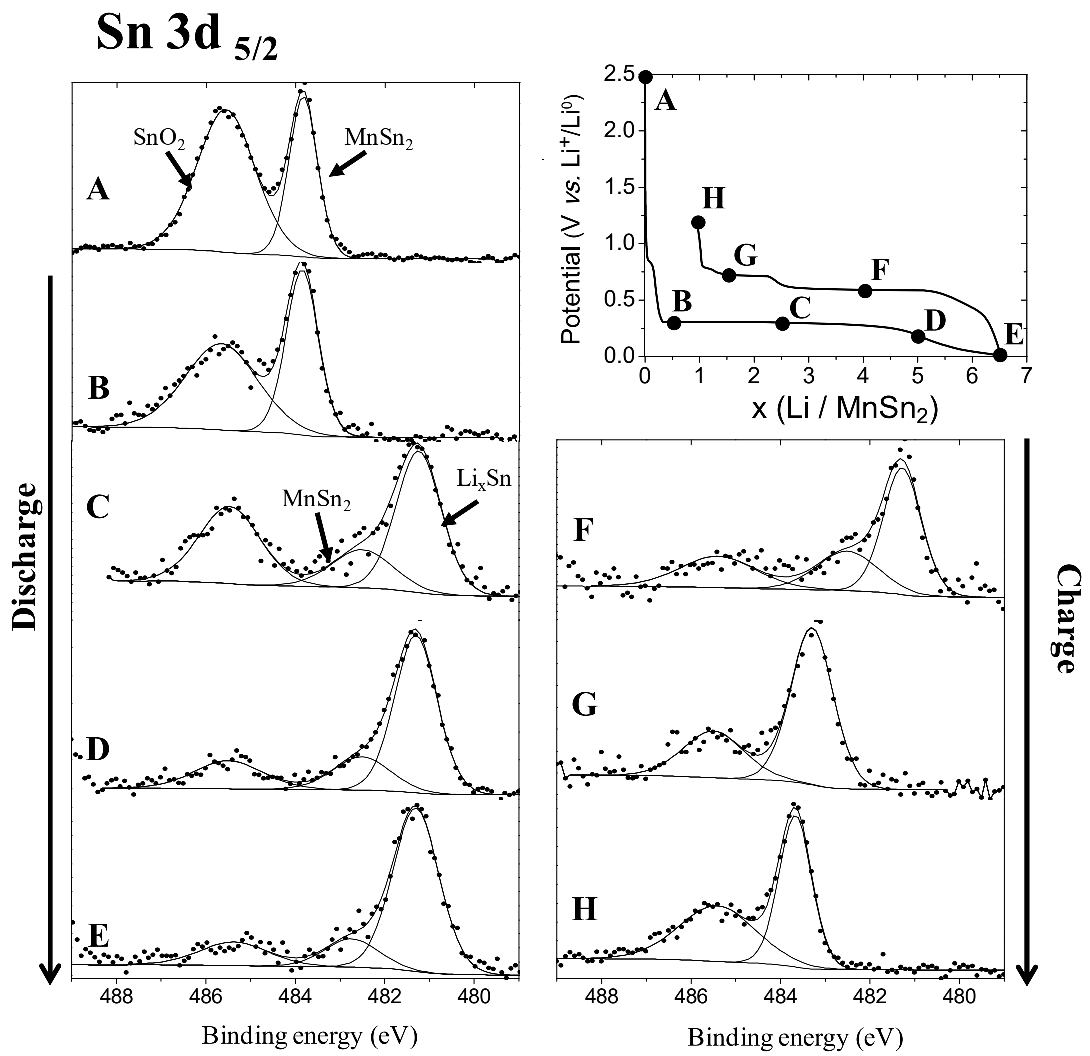

Figure 8: XPS Sn $3d_{5/2}$ spectra of the $MnSn_2$ electrode at different steps of the first discharge/charge cycle. Corresponding points are reported in the electrochemical potential curve (hν=1486.6 eV).

For sample C the relative proportion of Li-Sn alloy is greater than expected by the conversion reaction for x=2.5 Li, and from sample C to the end of discharge (sample E, x=6.5 Li) the $MnSn_2$ / Li-Sn ratio only weakly changes, while a linear conversion of $MnSn_2$

into Li_7Sn_2 is expected. Since XPS is a surface sensitive tool, these results indicate that the surface of the aggregates is lithiated earlier than the bulk upon the first discharge. Finally, at the end of discharge the $MnSn_2$ / Li-Sn ratio is 17/83, which is rather close to the expected value for a 6 Li low voltage plateau with respect to reaction (2). It is also worth noting that the relative amount of tin oxide at the surface continuously decreases over the whole discharge, whereas reduction of the surface oxide by lithium is expected at the beginning of discharge. This result can be related to magnetic measurements discussed above, suggesting that Mn nanoparticles formed upon discharge react with oxygen atoms found at the surface of the $MnSn_2$ particles.

Due to the small size and the rather poor crystallinity of the particles obtained at the end of discharge, no reliable information could be extracted from *operando* XRD patterns collected upon the first charge. However, additional results can be obtained from ^{119}Sn Mössbauer spectroscopy which is sensitive to the local environment of tin atoms. Some selected spectra are shown in Figure 9 with the corresponding points on the charge curve. About 6 Li have been extracted from the $MnSn_2$ electrode material with the modified Swagelok cell for *operando* Mössbauer measurements. The irreversibility of about 2 Li is due to both irreversible electrochemical reactions and the loss of electrical contacts between the particles of the powdered composite electrode within the cell. The Mössbauer spectra progressively change from a single peak mainly due to Li_7Sn_2 and to a small contribution of $MnSn_2$, as explained above, to a doublet at the end of the first plateau (x=3.4 Li) (Figure 9a). Among the different strategies we tried to fit the spectra, the best results were obtained by considering (i) one doublet with fixed Mössbauer parameters attributed to $MnSn_2$, which is present at the beginning of the charge, (ii) one doublet with fixed Mössbauer parameters attributed to Li_7Sn_2 which is the only lithiated tin based specie at the beginning of the charge and (iii) one doublet with free Mössbauer parameters which is attributed to one or more delithiated tin based phases due to the delithiation of Li_7Sn_2.

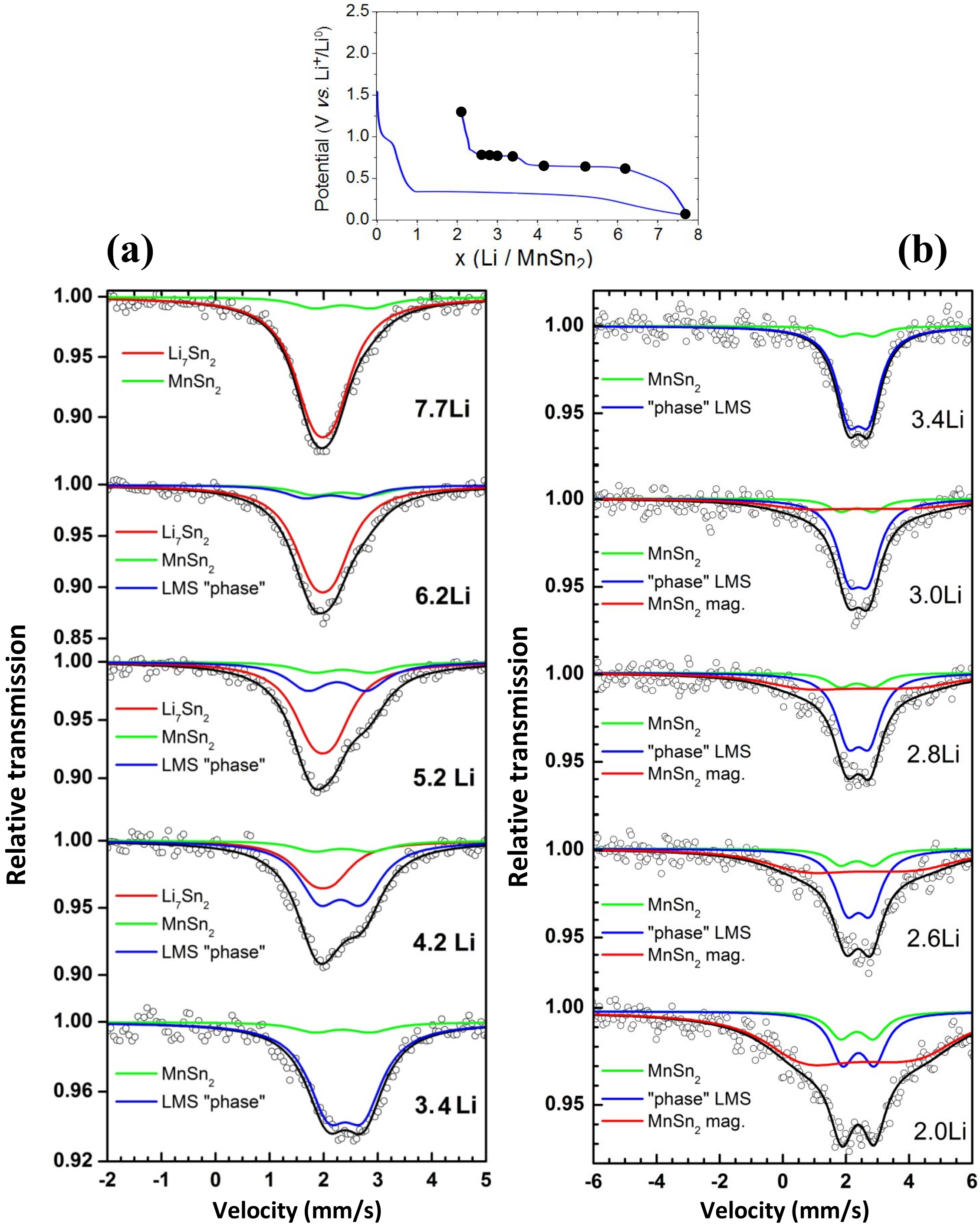

Figure 9: ^{119}Sn Mössbauer data recorded in *operando* mode at room temperature upon the first charge of a $MnSn_2$ // Li cell: **(a)** First voltage plateau, **(b)** Second voltage plateau. Corresponding points are reported in the electrochemical potential curve.

The latter doublet could be due to Li_xSn phases with $x<3.5$ and/or to ternary phases containing Li, Mn and Sn atoms since the values of the Mössbauer isomer shift are expected to be in the same range for those two types of Sn^0 based species. Thus, the Mössbauer parameters of this doublet (labelled "LMS phase" in Fig. 9) reflect averaged values for tin in different species formed from the delithiation of Li_7Sn_2 with a possible reaction with Mn nanoparticles. The Mössbauer spectra obtained for electrode compositions corresponding to the second potential plateau show that the doublet is transformed into a more complex spectrum with a strong broadened component (Figure 9b). In this case, a similar strategy to that of the first plateau was used to fit the spectra except for the Li_7Sn_2 component which was not considered since its contribution is negligible at the end of the first plateau. In addition, a third doublet was included to take into account the strong broadening of the spectra.

The variations of the relative sub-spectra areas show that the contribution of unreacted $MnSn_2$ is constant during the charge (Figure 10a). The contribution of Li_7Sn_2 decreases down to about zero at the end of the first plateau whereas that of the delithiated tin based phases increases up to about 90%. The observed strong non-linear variations could be due to the existence of different delithiated tin based phases and/or to changes in the Lamb-Mössbauer factors. Then, the contribution of the delithiated tin based phases decreases along the second plateau whereas that of the broadened component increases.

The variations of the values of δ and Δ for the delithiated tin based phases are shown in Figure 10b. The isomer shift increases from 1.9 to 2.3 mm/s as a function of the number of extracted lithium for the first plateau and then becomes constant for the second plateau. Increase of δ indicates that Sn 5s electron population increases on average and/or Sn 5p electron population decreases along the charge.[43] This was observed and explained, for example, in the series of Li_xSn compounds with decreasing x and the value $\delta = 2.3$ mm/s corresponds to Li-poor phases.[44] However, a similar trend could also be due to ternary Li-Mn-Sn phases since in the extreme situation of $MnSn_2$ the isomer shift (2.3 mm/s) is higher than that of Li_7Sn_2.

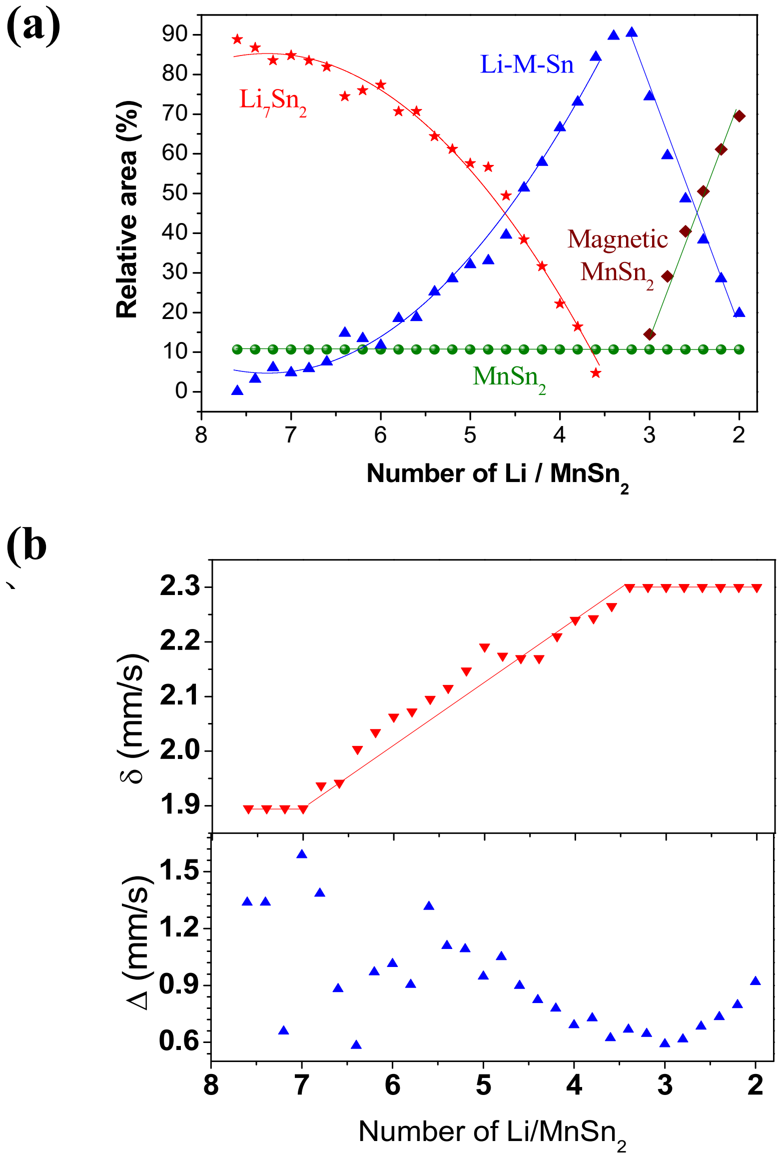

Figure 10: ^{119}Sn Mössbauer data recorded upon the first charge: **(a)** Relative sub-spectrum areas of the different phases in the electrode material, **(b)** Hyperfine parameters (isomer shift δ and quadrupole splitting Δ) of the delithiated Sn-based phase (denoted by Li-M-Sn). The lines are a guide for the eye.

The existence of β-Sn (complete delithiation) or nanocrystalline $MnSn_2$ (complete back reaction with Mn particles) at the end of the first plateau is excluded because in the former case the isomer shift is 2.56 mm/s and in the latter case the quadrupole splitting is 1.1 mm/s, which does not correspond to the observed values. There is no clear trend in the variations of the quadrupole splitting along the charge which is in the range 0.6-1.5 mm/s. The observed strong changes at the beginning of the charge for x>6 Li are probably due uncertainties in fitting procedure because of the small contribution of this component in this range of x. Rather high values of Δ reflect the asymmetry of the Sn 5p electron population due to asymmetric Sn local environments. Such values have been observed for some Sn crystallographic sites of the Li_xSn compounds [44] but this could also be due to the existence of Mn in the environment of Sn. Since the values of the Mössbauer parameters are averaged over the tin species within the electrode (except for $MnSn_2$ and Li_7Sn_2 end-members), these results indicate that the first plateau is due to the delithiation of Li_7Sn_2 without the progressive formation of the Li_xSn compounds or the direct transformation into $MnSn_2$. This suggests the formation of more complex metastable Li-poor Li-Sn and/or Li-Mn-Sn ternary phases. For the second plateau, the constant value of δ and the decreasing contribution of this doublet indicate a direct transformation of the Li-poor tin based phases. The strong broadening of the spectra suggests the existence of a magnetic hyperfine field at the Sn nucleus that could only originate from field transfer from Mn first-nearest neighbors as observed in antiferromagnetic bulk $MnSn_2$.[35] It is difficult to have an accurate characterization of this phase from our Mössbauer data which do not show well defined magnetic structures. The observed broadening of the doublet could be related to distributions of quadrupole splittings and hyperfine fields due to variations in the composition or the size of the Mn-Sn based particles and to relaxation effects. However, the Mössbauer spectrum at the end of charge looks like that of bulk $MnSn_2$, if we consider broadening effects, since the values of the isomer shift (2.3 mm/s) and the doublet splitting due to magnetic interactions (3.5 mm/s) are consistent with those observed for bulk $MnSn_2$ at room temperature. The variations of the relative areas of the sub-spectra of the Li-poor tin based phases and magnetic phases clearly indicate that the former ones are transformed into the latter ones during the delithiation. At the end of the charge, the electrode is mainly formed of “magnetic $MnSn_2$” but also contains some paramagnetic unreacted $MnSn_2$ and poorly lithiated Li-Mn-Sn phases. To our knowledge, this is the first observation of the appearance of a Sn hyperfine magnetic field in tin based intermetallic electrode materials due to electrochemical reactions with Li.

Concerning the XPS characterization of the charge (Fig. 8), the surface of sample F (x=4 Li, middle of first charge plateau) is rather similar to sample C (middle of discharge plateau, x=2.5 Li), except for the intensity of the tin oxide component which remains much lower upon charge. At this stage the $MnSn_2$ component remains smaller than that of the Li-Sn alloy. When the second charge plateau is reached (sample G, x=1.5 Li) the Li-Sn alloy component disappears from the spectrum, being replaced by that of delithiated tin which could be assigned to surface of Li-poor tin based phases and $MnSn_2$ as observed from Mössbauer spectroscopy. Finally at the end of charge (from G to H) no changes are observed in the Sn $3d_{5/2}$ spectrum, suggesting that the mechanism involving tin atoms at surface is complete. Unfortunately no information could be extracted from Mn 2p spectra because the electrode surface is rapidly covered by an SEI film after x=1 Li upon discharge and because the XPS cross section of Mn 2p core peak is too low to make manganese observable in these conditions.

3.2.2. Electrode/electrolyte interface

a) Covering process by the SEI

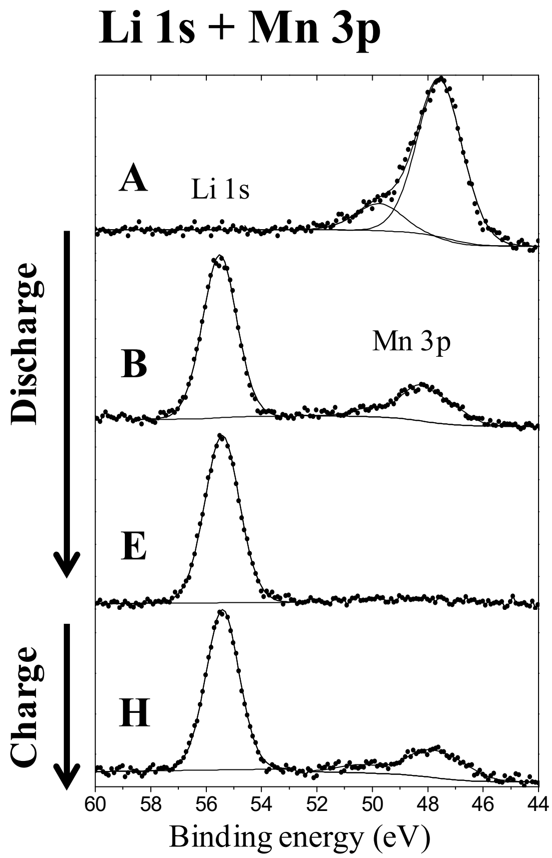

Figure 11: XPS Li 1s and Mn 3p spectra of the $MnSn_2$ electrode at different steps of the first discharge/charge cycle: E = end of discharge, H = end of charge (hν=1486.6 eV).

Figure 11 shows Li 1s and Mn 3p spectra of the $MnSn_2$ electrode at different steps of the first discharge/charge cycle. The decrease and disappearance of the Mn 3p peak and the increase of the Li 1s peak upon discharge mean that the electrode material (containing Mn) is being covered by a thick surface layer (the SEI) containing lithiated compounds. Therefore, the observed combined changes in these two core-level spectra are a good indicator of the formation of the SEI. Note that the Mn 3p peak weakly reappears at the end of charge (sample

H), which means a decrease of the SEI thickness upon charge (partial re-dissolution process of the SEI). The binding energy value of Li 1s peak (55.6 eV) is in good agreement with the main lithiated compounds expected at the surface, *i.e.* Li_2CO_3 (55.5 eV) and LiF (56 eV), which are degradation compounds of the solvent and of the salt, respectively.

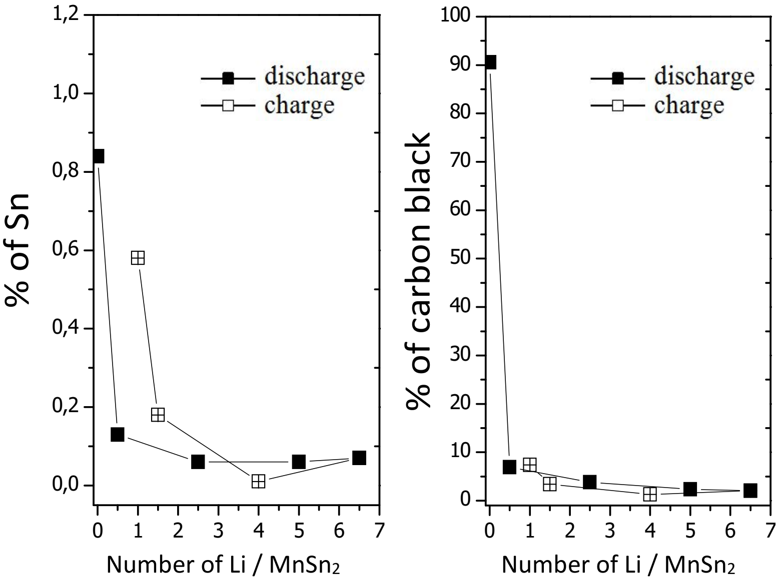

Figure 12: Atomic % of tin and carbon black as measured by XPS at the surface of $MnSn_2$ composite electrodes upon the first discharge/charge cycle (hν=1486.6 eV).

Figure 12 shows the evolution of the total amount (atomic %) of tin and carbon black measured at the surface of the $MnSn_2$ electrode from Sn $3d_{5/2}$ and C 1s XPS spectra upon the first electrochemical cycle. Tin and carbon black (conductive additive) are species found in the electrode but not in the SEI and consequently the atomic percentages of these species at the surface are good indicators of the thickness of the SEI covering the particles. This means that covering the surface by the SEI will result in a decrease of the signals of the electrode.

The atomic percentage of carbon black at the pristine electrode surface (sample A) is very high (90%) compared to its actual mass content in the electrode (10%), because it acts as a carbon nano-painting covering $MnSn_2$ particles. Therefore the measured atomic percentage of tin at the pristine electrode surface is very low (~0.8%). At the beginning of the first discharge (between 0 and 0.5 Li) the amounts of tin and carbon black dramatically fade to 0.13% and 6.9% respectively. Then, they slowly decrease until the end of discharge. Similar results were obtained for Ni_3Sn_4 [41] and $FeSn_2$.[12,45] This shows that the SEI mainly forms at the beginning of the discharge (potential > 0.3 V vs. Li^+/Li), and that its thickness slowly increases in the following steps of the discharge. The formation of this layer is mainly irreversible since the percentages of tin and carbon black are lower at the end of charge (sample H) than at the beginning of discharge (sample A). However a partial re-dissolution process of the SEI is observed since the atomic % of tin and carbon black re-increase upon charge.

b) Composition of the SEI

XPS analysis of C 1s core peaks of the $MnSn_2$ electrode upon the first discharge did not show any significant change of the composition of the SEI in carbonaceous species. [25]

Information about inorganic species can be extracted from other XPS core peaks. Figure 13 shows the evolution of the O 1s, F 1s and P 2p spectra of the $MnSn_2$ electrode upon the first discharge/charge cycle ($h\nu = 1486.6$ eV). The O 1s spectrum of the pristine electrode (sample A) consists of a peak at 530.4 eV assigned to the manganese and tin surface oxides and another peak at 532.0 eV attributed to oxygenated species adsorbed at the surface of the pristine electrode. No signal is observed for F 1s and P 2p core peaks since this sample has not yet been in contact with the electrolyte. After reaction with 0.5 Li (sample B), the SEI is already formed as shown in Figure 12. As a result various oxygenated species are present on the particle surfaces and in the SEI layer. The O 1s spectrum of sample B consists of a main component at 531.7 eV and a component of low intensity at higher binding energy (~533.5 eV).

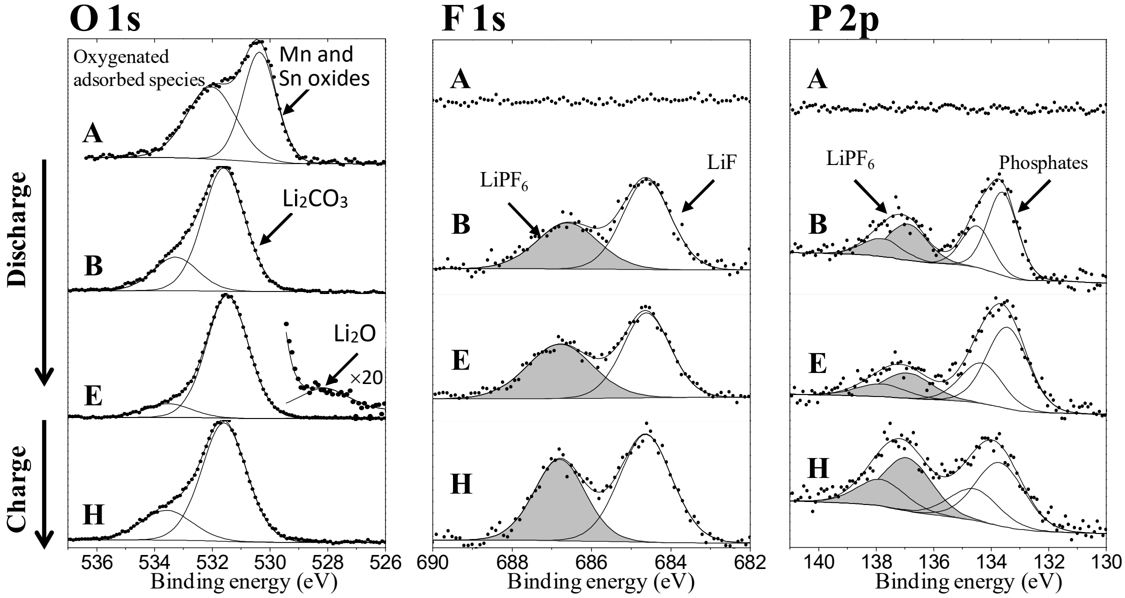

Figure 13: XPS O 1s, F 1s and P 2p spectra of the $MnSn_2$ electrode at different steps of the first discharge/charge cycle. A = pristine powder, B = 0.5Li, E = end of discharge, H = end of charge (hν=1486.6 eV).

These two signatures correspond to carbonates, alkyl carbonates and other organic species commonly found in SEI with carbonates solvents. [46,47,48] As they are due to the electrochemical degradation of the solvents present in the electrolyte, similar species have been observed on surfaces of graphite, Si or Sb intermetallic electrodes. [42,49,50] It is worth to note that the O 1s peak relating to tin and manganese oxides disappears totally. According to the thickness of the SEI and its rich nature in oxygenated species, the signature of the oxides of the pristine materials might not be detected. The reduction process of surface tin oxide has also to be considered. At the end of the discharge (E) and of the charge (H), the same two main peaks are observed.

At the end of the discharge (E) a very weak O 1s component attributed to Li_2O (528.2 eV) is hardly detectable (zoom ×20 in Fig. 14). The formation of Li_2O is known as resulting from the reduction of oxide, especially tin oxide, from the pristine material surface. Interestingly, the intensity of the Li_2O component is much weaker than that previously observed for other tin-transition metal alloys such as Cu_6Sn_5 or Ni_3Sn_4 [41] or silicon electrodes [42] recorded in similar conditions. The absence of Li_2O may be explained by the presence of oxidized manganese nanoparticles at the end of discharge, as discussed above.

The F 1s spectra consist of two peaks. The first one at 684.7 eV (in white) corresponds to lithium fluoride LiF, a major degradation product of the salt $LiPF_6$. The second one at 686.8 eV (in grey) is attributed to PF_6^- anions taking part in the SEI composition (rather than traces of $LiPF_6$ salt remaining at the surface of the electrodes after washing with DMC solvent). The overall shape of the F 1s spectra is stable over the whole electrochemical cycle, and the measured amount of LiF remains rather low (between 1 and 3 at.%).

The P 2p spectra also consist of two peaks; a first one at 137 eV (in grey) attributed to PF_6^- anions, and a second at 133.7 eV assigned to phosphates which come from the degradation of $LiPF_6$ and are commonly found in the SEI. As previously, the overall shape of the spectra is stable during the first electrochemical cycle of the cell and the amount of phosphates also fluctuates between 1 and 3 at.% of the SEI.

As a summary, the formation of the SEI on $MnSn_2$ electrode mainly occurs at the beginning of the first discharge and its composition remains remarkably stable over the first cycle. The covering of the SEI increases upon discharge and slightly decreases upon charge.

4. Conclusion

In this work we have investigated the mechanisms undergone by a $MnSn_2$ electrode upon lithiation/delithiation during the first cycle in a Li//$MnSn_2$ electrochemical cell. The electrochemical cycle is characterized by one voltage plateau upon discharge and two plateaus upon charge. These voltage plateaus could be attributed to complex electronic and structural mechanisms. Lithium insertion into $MnSn_2$ during the discharge leads to the formation of a nanocomposite consisting of Li_7Sn_2 and of Mn nanoparticles. These Mn nanoparticles are highly reactive and immediately oxidized at their surface, by reaction with oxygen from the solvent molecules and/or from the pristine $MnSn_2$ surface oxide layer.

Lithium extraction from this nanocomposite during the first part of the charge leads to the delithiation of Li_7Sn_2 and the formation of Li-poor Li-Sn and/or Li-Mn-Sn phases, without recovery of $MnSn_2$. During the second part of the charge, further de-lithiation leads to the formation of magnetic $MnSn_2$ particles and to our knowledge it is the first time such a mechanism is observed in tin based intermetallic electrode materials due to electrochemical reactions with Li.

Concerning the electrode/electrolyte interface, the SEI layer is formed at the beginning of the first discharge. Further discharge leads to the slight increase of the SEI thickness. During charge, a partial re-dissolution process of the SEI is visible. Over the whole first electrochemical cycle, the SEI layer chemical composition is very stable and very similar to that observed for a graphite or Si-based electrode when a similar electrolyte is used.

Acknowledgements

This work was carried out in the framework of Alistore European Research Institute. The authors are grateful to the European Community for financial support. The authors are also grateful to the French Education and Research Ministry and to StandUp for Energy, the Swedish Research Council VR and the Swedish Energy Agency. A. Mahmoud acknowledges the support from the Agence Universitaire de la Francophonie (AUF). Finally, the authors would like to thank Mihaela Gorgoi for her support at Bessy II synchrotron, Mohamad Chamas for his help in sample preparation, XRD and Mössbauer experiments and Corine Reibel for the magnetic measurements.

References

(1) H. Li, Z. Wang, L. Chen, X. Huang, *Adv. Mater.* **2009**, *21*, 4593-4607.

(2) B. Scrosati, J. r. Garche, *J. Power Sources* **2010**, *195*, 2419-2430.

(3) A. N. Dey, *J. Electrochem. Soc.* **1971**, *118*, 1547-1549.

(4) J. Wang, I. D. Raistrick, R. A. Huggins, *J. Electrochem. Soc.*, **1986**, *133*, 457.

(5) R. A. Huggins, C. J. Wen, *J. Electrochem. Soc.* **1981**, *128*, 1181-1187.

(6) S. Naille, C. M. Ionica-Bousquet, F. Robert, F. Morato, P.-E. Lippens, J. Olivier-Fourcade, *J. Power Sources* **2007**, *174,* 1091-1094

(7) M. Winter, J. O. Besenhard, *Electrochim. Acta* **1999**, *45*, 31-50.

(8) M. Wachtler, J. O. Besenhard, M. Winter, *J. Power Sources* **2001**, *94*, 189-193.

(9) S. Naille, M. Mouyane, M. Amraoui, P.-E. Lippens, J.-C. Jumas, J. Olivier-Fourcade, *Hyperfine Interact.* **2008**, *187*, 19-26.

(10) R. Hu, M. Zeng, C. Y. V. Li, M. Zhu, *J. Power Sources* **2009**, *188*, 268-273.

(11) O. Mao, R.A. Dunlap, J. R. Dahn, *J. Electrochem. Soc.* **1999**, *146*, 405

(12) M. Chamas, P.-E. Lippens, J.-C. Jumas, K. Boukerma, R. Dedryvère, D. Gonbeau, J. Hassoun, S. Panero, B. Scrosati, *J. Power Sources* **2011**, *196*, 7011

(13) I. Amadei, S. Panero, B. Scrosati, G. Cocco, L. Schiffini, *J. Power Sources* **2005**, *143*, 227-230

(14) X.-Q. Cheng, P.-F. Shi, *J. Alloys Comp.* **2005**, *391*, 241-244

(15) S. Naille, P.-E. Lippens, F. Morato, J. Olivier-Fourcade, *Hyperfine Interact.* **2006**, *167*, 785.

(16) M.-Z. Xue, Z.-W. Fu, *Solid State Ionics* **2006**, *177*, 1501-1507

(17) K. Kepler, J. Vaughey, M. M. Thackeray, *Electrochem. Solid-State Letts.* **1999***, 2,* 307-309.

---

(18) E. Nordström, S. Sharma, E. Sjöstedt, L. Fransson, L. Häggström, L. Nordström, K. Edström, *Hyperfine Interact.* **2001**, *136-137*, 555-560

(19) S. Sharma, L. Fransson, E. Sjöstedt, L. Nordström, B. Johansson, K. Edström, *J. Electrochem. Soc.* **2003**, *150*, A330-A334.

(20) S. Naille, R. Dedryvère, S. Leroy, H. Martinez, P.-E. Lippens, J.-C. Jumas, D. Gonbeau, *J. Power Sources* **2007**, *174*, 1086

(21) L. Beaulieu, D. Larcher, R. A. Dunlap, J. R. Dahn, *J. Alloys Comp.* **2000**, *297*, 122-128

(22) P. P. Ferguson, M. L. Martine, A. E. George, J. R. Dahn, *J. Power Sources* **2009**, *194*, 794-800

(23) M. M. Thackeray, J. T. Vaughey, C. S. Johnson, A. J. Kropf, R. Benedek, L. Fransson, K. Edström, *J. Power Sources* **2003**, *113*, 124-130

(24) L. Fransson, E. Nordström, K. Edström, L. Häggström, J. T. Vaughey, M. M. Thackeray, *J. Electrochem. Soc.* **2002**, *149*, A736-A742

(25) A. Mahmoud, M. Chamas, J.-C. Jumas, B. Philippe, R. Dedryvère, D. Gonbeau, I. Saadoune, P.-E. Lippens, J. Power Sources **2013**, *244*, 246-251

(25) J. B. Leriche, S. Hamelet, J. Shu, M. Morcrette, C. Masquelier, G. Ouvrard, M. Zerrouki, P. Soudan, S. Belin, E. Elkaïm, F. Baudelet, *J. Electrochem. Soc.* **2010**, *57*, A606

(26) M. Chamas, M.T. Sougrati, C. Reibel, P. E. Lippens, *Chem. Mater.* **2013**, *23*, 2410-2420.

(28) J. Rodriguez-Carvajal, FULLPROF version January 2006, Laboratoire Léon Brillouin, http://www-llb.cea.fr/fullweb/powder.htm

(29) K. Ruebenbauer, T. Birchall, *Hyperfine Interact.* **1979**, *7*, 125-133

(30) D. A. Shirley, *Phys. Rev. B* **1972**, 5, 4709−4714.

(31) J. H. Scofield, *J. Electron Spectrosc. Relat. Phenom.*, **1976**, *8*, 129-137

(32) M. Gorgoi, *Nucl. Instrum. Methods Phys. Res., Sect. A* **2009**, *601*, 48.

---

(33) F. Schaefers, M. Merlin, M. Gorgoi, *Rev. of Scientific Instruments* **2007**, 78, 123102

(34) Y. Dong, F. J. DiSalvo, *Acta Cryst.* **2005**, *E61*, 282

(35) G. Le Caër, B. Malaman, G. Venturini, I. B. Kim, *Phys. Rev.* **1982**, *B26*, 5085

(36) R. Benedek, M. M. Thackeray, *J. Power Sources,* **2002**, *110*, 406-411

(37) J. Wolfenstine, S. Campos, D. Foster, J. Read, W. K. Behl, *J. Power Sources* **2002**, *109*, 230-233

(38) C. M. Bousquet, P. E. Lippens, L. Aldon, J. Olivier-Fourcade, J.-C. Jumas, *Chem. Mater.* **2006**, *18*, 6442-6447

(39) P. Z. Si, E. Brück, Z. D. Zhang, O. Tegus, W. S. Zhang, K. H. J. Buschow, J. C. P. Klaasse, *Mater. Res. Bull.*, **2005**, *40*, 29-37

(40) S. Naille, R. Dedryvère, D. Zitoun, P.-E. Lippens, *J. Power Sources* **2009**, *189,* 806-808.

(41) K. K. D. Ehinon, S. Naille, R. Dedryvère, P-E. Lippens, J-C. Jumas, D. Gonbeau, *Chem. Mater.* **2008**, *20*, 5388-5398.

(42) B. Philippe, R. Dedryvère, J. Allouche, F. Lindgren, M. Gorgoi, H. Rensmo, D. Gonbeau, K. Edström, *Chem. Mater.* **2012**, *24*, 1107–1115.

(43) P.-E. Lippens, *Phys. Rev. B* **1999**, *60*, 4576

(44) F. Robert, P.-E. Lippens, J. Olivier-Fourcade, J.-C. Jumas, F. Gillot, M. Morcrette, J.-M. Tarascon, *J. Solid State Chem.* **2007**, *180*, 339

(45) M. Chamas, P.-E. Lippens, J.-C. Jumas, J. Hassoun, S. Panero, B. Scrosati, *Electrochimica Acta* **2011**, *56*, 6732

(46) D. Aurbach, M. L. Daroux, P. W. Faguy, E. Yeager, *J. Electrochem. Soc.* **1987**, *134*, 1611-1620

(47) A. M. Andersson, K. Edström, *J. Electrochem. Soc.* **2001**, *148*, A1100-A1109

---

(48) S. Verdier, L. El Ouatani, R. Dedryvère, F. Bonhomme, P. Biensan, D. Gonbeau, *J. Electrochem. Soc.* **2007**, *154,* A1088-A1099

(49) S. Leroy, F. Blanchard, R. Dedryvère, H. Martinez, B. Carré, D. Lemordant, D. Gonbeau, *Surf. Interfa. Analysis* **2005,** 37, 773-781.

(50) M. Stjerndahl, H. Bryngelsson, T. Gustafsson, J. T. Vaughey, M. M. Thackeray, K. Edström, *Electrochim. Acta* **2007**, *52*, 4947-4955.